

Dielectric waveguide setup tested with a superconducting millimeter-wave Fabry-Pérot interferometer at milli-Kelvin temperatures

J. Lenschen, R. Labbe, N. Drotleff, M. Fuhrmann, and J. Lisenfeld
Physikalisches Institut, Karlsruher Institut für Technologie

H. Rotzinger and A.V. Ustinov
*Physikalisches Institut, Karlsruher Institut für Technologie and
Institut für Quantenmaterialien und Technologie, Karlsruher Institut für Technologie**
(Dated: November 22, 2024)

We proposed and tested a cryogenic setup comprising dielectric waveguides for mm-wave frequencies in the range of 75 – 110 GHz and temperatures down to 10 mK. The targeted applications are quantum technologies at millimeter-wave frequencies, which require measurements at low photon numbers and noise. We show that the high density polyethylene waveguides combine a frequency independent low photon loss with a very low heat conductance. Black high density polyethylene shows a higher attenuation, which is useful to block thermal photons in a cryogenic environment. The dielectric waveguides are thermally anchored and attenuated at several stages of the cryostat. They are individually protected by additional metallic shields to suppress mutual cross-talk and external interference. We have measured a Fabry-Pérot cavity with superconducting mirrors at 10 mK and found out that the quality of a signal transmitted through the dielectric waveguides is sufficient to measure resonator quality factors over one million at 110 GHz.

I. INTRODUCTION

Millimeter wave measurements at ultra low temperatures are widely unexplored due to several technical difficulties including, for instance, a challenging signal path thermalization and isolation. The tremendous progress in quantum computing at microwave frequencies seen over the last two decades did not so far approach the mm-wave range. The mm-wave quantum measurements would profit from an order of magnitude larger photon energy, wider bandwidth, enhanced resilience against thermal fluctuations, and may speed up qubit manipulation.

The traditionally used metallic hollow waveguides are very good conductors of mm-wave signals but are not flexible and cause an intolerable heat load on the cryogenic temperature stages. Also, the transmission of thermal radiation from elevated temperature stages can be problematic due to opening path to excess flux of infrared photons which heat up the low-temperature stages. Here, we propose an alternative approach to 100 GHz range quantum measurements by using dielectric waveguides (DWGs) to transmit mm-wave signals from room to milli-Kelvin temperatures and back. DWGs offer several advantages: An ultra low heat conductance, very good transmission properties, and can be easily thermalized. Furthermore, DWGs exhibit very good mechanical flexibility and offer several options to handle the attenuation and suppression of infrared radiation. Although it was long known that a dielectric strip can carry mm-waves [1], practical investigations motivated by advances in information technology were carried out only about

one decade ago [2] and are still an attractive area of developments [3]. Very recent usage of DWGs for cryogenic applications employed frequencies up to 300 GHz [4]. There, a circuit board was used to bridge the temperature stages of a cryostat to a base temperature of 4.2 K.

In this paper, we describe a cryogenic setup including DWG signal lines with a high signal attenuation at the input and a low signal attenuation at the output lines. We also report on testing the setup with a superconducting Fabry-Pérot interferometer and observation of high-Q resonances in the W-band (75-110 GHz).

II. ULTRA-LOW TEMPERATURE MILLIMETER-WAVE SETUP

The developed cryogenic mm-wave setup consists of four main parts: A commercial pulse tube pre-cooled dilution refrigerator (Blufors LD250) with a base temperature of 10 mK, a mm-wave vacuum-transition, black and transparent DWGs bridging the temperature stages and a low noise amplifier with an isolator located at the 2.7 K stage. Pre-characterization measurements are also carried out in a home-made dry refrigerator with a base temperature of 2.4 K (TransMIT 2-stage pulse-tube type PtQUBE). The Fabry-Pérot cavity, discussed in the second part of the paper, is directly connected to the DWGs, see Fig. 1 for a schematic representation. All presented measurements are carried out at room temperature using a Rhode & Schwarz ZNA67 vector network analyzer (VNA) with external W-band extenders (ZC110).

* rotzinger@kit.edu

A. Vacuum transition

We use one standard KF40 flange on the top of the fridge to add a vacuum tight box equipped with four copper WR10 waveguides. Each feed-through of the flange is closed by an o-ring sealed stainless steel metal plate which hosts the vacuum transition between two WR10 waveguides. The waveguides are connected with UG-387/UM connectors from the in- and outside of the flange. We seal the spark-eroded rectangular waveguide hole in the metal plate with a 100 μm thick polyimide foil and an o-ring, see inset in Fig. 1 for a schematic. The helium leak rate of the box was measured to be 5×10^{-8} mbar \cdot l/s, confirming the reliability of the polyimide/o-ring seal. A similar approach was proposed previously by [5]. Transmission measurements reveal an average attenuation of -4 dB and reflection below -10 dB over the full spectrum, see Fig. 3. While these values are sufficient for the planned measurements, further optimizations towards increasing the transmission, e.g. by using a thinner polyimide or mica foil, are possible. Also, no special attention was devoted to the suppression of standing waves in the transition plate, see e.g. [5] for a detailed discussion on this matter.

B. Dielectric waveguides

DWGs, like optical fibers, rely on the principle of total internal reflection which emerges when the carrying medium (the DWG) has a substantially different dielectric constant (or refraction index) than its environment. In our approach, we use a rectangular strip of high density polyethylene (HDPE) with a dielectric constant $\epsilon_r = 2.33$ [6] embedded in a round polyethylene (PE) foam tube with a diameter of 14 mm ($\epsilon_r < 1.1$). We have chosen HDPE because of its reported low loss [7], flexibility at room temperature, low piezoelectricity and low temperature dependence of the dielectric constant. In addition, HDPE material shows a good inertness to many chemicals and low moisture sensitivity. The DWG are fabricated from black or transparent HDPE sheets that are cut to a width of 2.5 mm and then rolled to a thickness of 1.3 mm using an in-house made cutting tool, see Fig. A.1. The electromagnetic properties of the black and transparent DWGs are discussed below.

At mm-wave frequencies, the electromagnetic field of the signal is almost completely confined to the DWG, only a small evanescent field near the DWG's outer boundary is present. According to simulations [2], the evanescent electric field amplitude drops exponentially with about 6 dB/mm for a material with a comparable $\epsilon_r = 2.6$. DWG materials with a higher dielectric constants, like e.g. some glass reinforced plastics, could be beneficial in terms of a stronger confinement of the electric field. Considering a DWG made from a material with an $\epsilon_r = 6.15$, the surface electric field should drop of by 23 dB/mm [2].

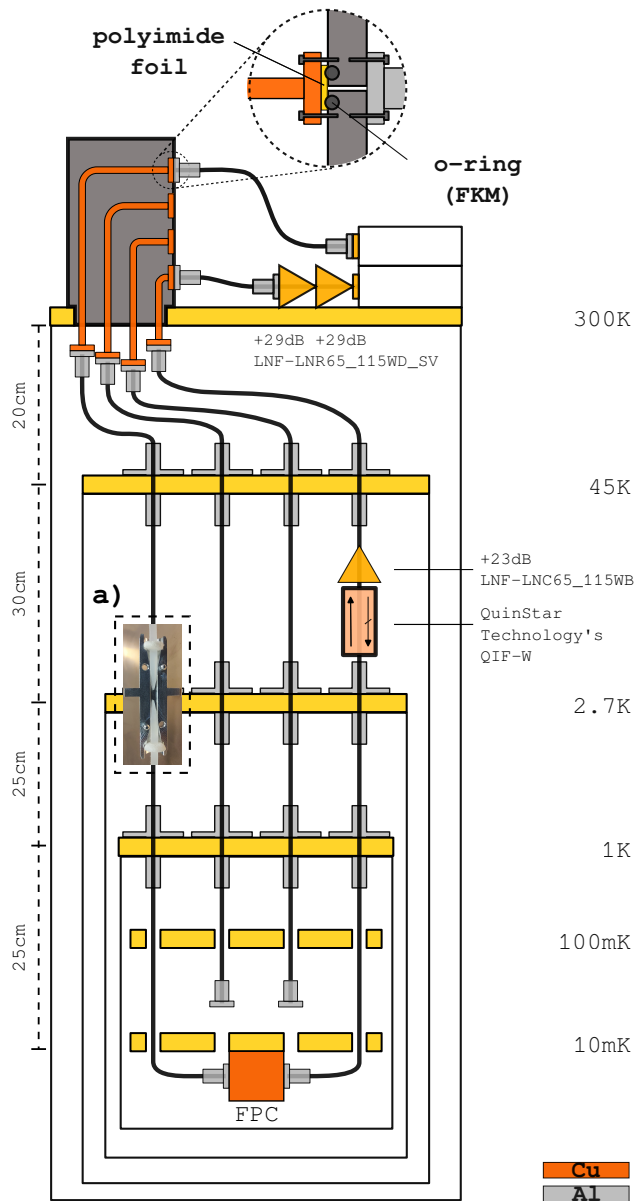


FIG. 1. Schematic of the cryogenic setup with added DWGs. The VNA connect to the four-port vacuum transition (left) which uses a polyimide foil and an o-ring to ensure vacuum tightness. Copper waveguides connect to the DWGs, which are thermally anchored at every stage of the cryostat. The Fabry-Pérot cavity is located at 10 mK.

To suppress crosstalk between the lines guiding the signal to and from the low-temperature stage, we place an additional metal shield around the PE foam, see Fig. 2. This is realized by a metal mesh to retain the flexible character of the DWG. The shield is especially mandatory at a high signal attenuation (> 30 dB) sections, since without the shield the higher crosstalk leads to significant signal distortion. A suitable material for the mesh shield is stainless steel, due to its low cryogenic heat conductance, see discussion below. We measure a cross-talk suppression exceeding 60 dB in the proposed configuration.

Other material solutions for the shield, like stainless steel belly-tubes or a conductive metalization on the outer side of the PE foam are also possible, but not considered here.

In order to increase signal attenuation and thus thermalization, we make use of the evanescent wave of the DWG by placing a dissipative coating (copper powder filled epoxy) on the dielectric at several positions, see section IIF for more details.

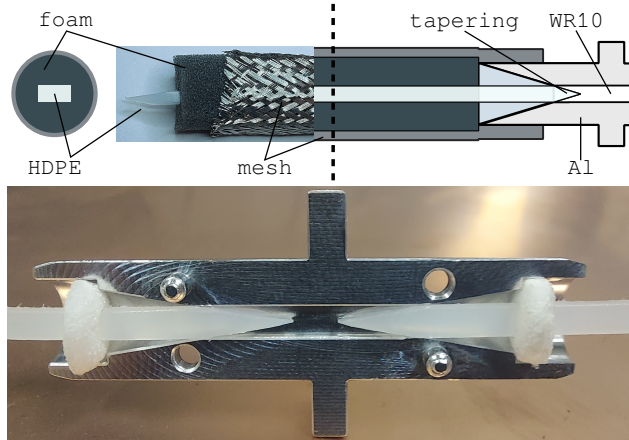


FIG. 2. **Top:** Cross sections of the DWG with added aluminum UG-387/UM flange adapter. The image shows a fully assembled DWG with shielding. **Bottom:** Picture of an open thermalization transition. The middle part consists of a WR10 waveguide in which the tapered ends of both dielectric waveguides lie. On either side the transition features cone-shaped openings in which two foam disks hold the dielectric waveguides in position while assuring electric decoupling.

To connect individual waveguides we developed an adapter with a UG-387/UM flange shown in Fig. 2. It is constructed out of two cone-shaped aluminum parts that are attached to the tapered ends of the dielectric. By the tapering, a convenient way of impedance matching between the WR10 waveguide and the DWG is provided that can be optimized individually for each transition [7] while the cone-shapes increase coupling to the evanescent portion of the wave, as proposed by [8]. The DWG is held in place by a disk of low loss foam with $\epsilon_r \approx 1.1$ (Millifoam DIV110U).

C. Room temperature properties of dielectric waveguides

Measurements of the mm-wave transmission through a DWG with varying bending radii show a clear picture, see Fig. 3. Independent of the orientation of the bending, above a radius of 1.5 – 2 cm the transmission remains independent of the bending radius. At smaller radii, the mm-wave loss increases significantly.

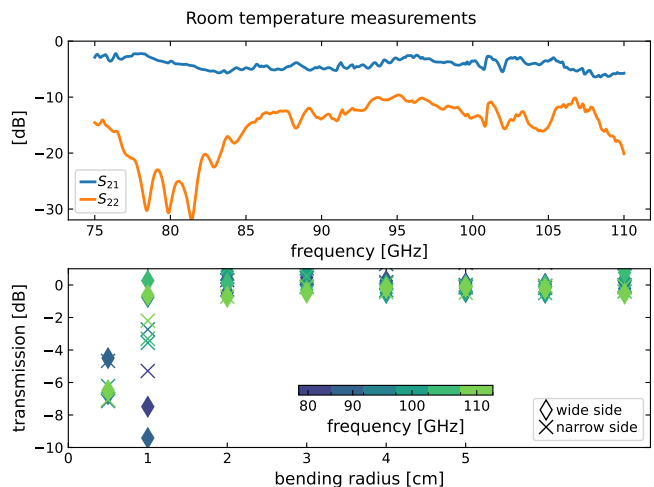


FIG. 3. **Top:** Transmission and reflection measurement of the vacuum transition. **Bottom:** Relative changes in attenuation for a waveguide bent by 180° with different bending radii. The waveguide under test is made without foam or shielding and consist of the bare dielectric.

D. Transmission properties of dielectric waveguides at cryogenic temperatures

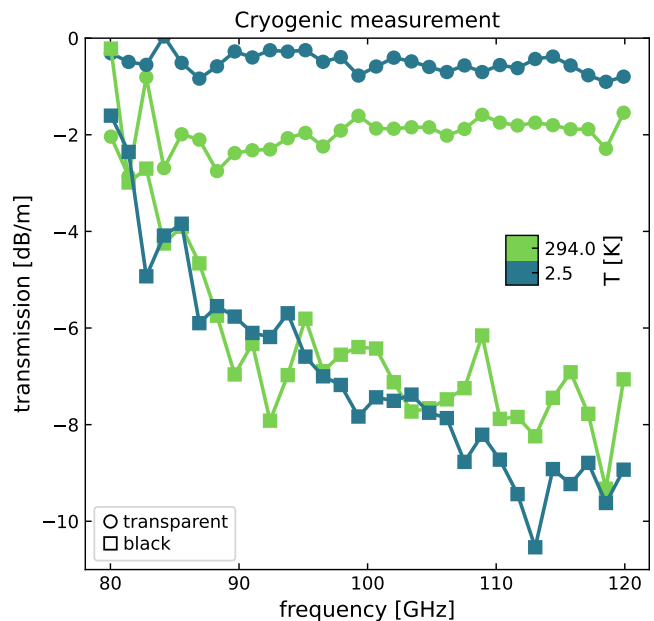


FIG. 4. Transmission of a 50 cm long transparent and a 25 cm black DWG at room temperature and at 2.5 K. The values are normalized to dB/m.

For the cryogenic characterization, we employ 50 cm (25 cm) long transparent (black) DWG samples with shielding and UG-387/UM adapters on both sides. Room temperature values are compared with measurements at 2.5 K. The setup was calibrated in several consecutive

cool down steps, with and without DWG samples. The data obtained by this procedure are used to de-embed the cable. Figure 2 shows the resulting transmission data. The used calibration setting is, however, sensitive to non-stationary influences, e.g. small changes of the DWG-to-adapter impedance matching. We attribute the residual oscillations with an amplitude periodicity of about 10 GHz to such an origin. Further, noise originating from the pulse tube pre-cooler is observed when measuring the high-Q resonators, see below. This noise is not present when the pre-cooler is switched off, so we suspect that the noise is caused by either vibrational or electrical interference.

The attenuation of the transparent DWG is roughly frequency independent and decreases with temperature leading to a transmission of about 1.5 dB/m at room temperature and 0.6 dB/m at 2.5 K. Interestingly, the black DWG shows, for frequencies above 95 GHz, a slightly higher attenuation at low temperature. Below this frequency, the attenuation of the black DWG seems unchanged. The origin of this effect is unknown, but it could hint towards an involvement of carbon as a HDPE filler material, which shows a strong temperature dependence in composite materials, e.g. in the electrical conductance [9].

The following conclusions can be drawn from above findings. First, both transparent HDPE and black HDPE materials are suitable for low temperature applications. For the transparent DWG, we find a very low cryogenic attenuation, which facilitates measurements of small signals, present for instance in quantum technologies. The stronger damping of the black DWG can be used to attenuate applied mm-wave signals, suppress the background thermal radiation from the high-temperature stages, and thus enhance the noise background at the cold sample under investigation. In addition, the black HDPE filling also reduces the influence of infrared radiation, originating from warmer stages of the cryostat.

E. Dielectric waveguide thermalization

For thermalization, the DWGs are intersected at the individual stages of the cryostat with metallic transitions using the following approach. The signal is coupled out of the dielectric waveguide into a hollow aluminum rectangular waveguide and vice versa. The coupling is achieved in a similar fashion to that described above for the UG-387/UM adapter. An inside-view of the transition piece, which is made from two identical parts that are screwed together, is shown in Fig. 2. A small drop of epoxy glue is used to secure the DWGs in position, which also enhances the thermal contact with the aluminum casing.

To get an estimate for the added heat load on the low temperature stages due to the DWGs, we use Fourier's definition of the heat flux in one dimension

$$Q/A = -\kappa \frac{dT}{dx} \approx -\bar{\kappa} \frac{\delta T}{\delta l} \quad (1)$$

where A , δl are the cross section and length of the heat conductor, respectively. The values for the average heat transfer coefficient $\bar{\kappa}$ are taken from tabulated data. Due to a lack of specific experimental data, the estimation does not distinguish between different variants of polyethylen (e.g. LDPE or HDPE) or color (transparent or black). We did not consider the detailed temperature gradient but instead use the temperature difference δT between the stages. The results are listed in Table I.

cryogenic stage	δl [cm]	δT [K]	$\bar{\kappa}_{PE}$ [$\frac{\mu W}{cm K}$]	$\bar{\kappa}_{SS}$ [$\frac{\mu W}{cm K}$]	DWG Q [μW]	DWG+S Q [μW]
45 K	17	248	$5 - 30 \cdot 10^3$ †	$5.2 \cdot 10^3$	1.4	1.8
2.7 K	28	42.3	100	$2.1 \cdot 10^3$	$4.9 \cdot 10^{-4}$	$1.4 \cdot 10^{-2}$
1 K	24	1.7	20	$1.5 \cdot 10^3$	$4.6 \cdot 10^{-6}$	$4.6 \cdot 10^{-4}$
500 mK	-	0.5	4	700	$6.5 \cdot 10^{-7}$	$1.5 \cdot 10^{-4}$
100 mK	15	0.9	1.5*	100*	$2.7 \cdot 10^{-7}$	$2.5 \cdot 10^{-5}$
10 mK	10	0.09	1.0*	40*	$2.9 \cdot 10^{-8}$	$1.6 \cdot 10^{-6}$

TABLE I. Estimated thermal heat load Q by the added DWGs at different stages of the cryostat. The values of the DWG+S include the DWG and the stainless steel mesh, the PE foam ($\rho = 24 \text{ mg/cm}^3$) was neglected. The 500 mK stage is added for reference only, we do not thermalize the DWGs there and at 100 mK only the outer shield. The tabulated values for stainless steel ($A = 4.4 \cdot 10^{-6} \text{ m}^2$) are taken from [9, 10], for HD-PE ($A_{\text{eff}} = 3.25 \cdot 10^{-6} \text{ m}^2$) from [11–13]. (†) The heat conductance of HDPE depends on the extrusion direction, see [11] for details. (*) Denotes extrapolated values.

The cooling power of today's dilution refrigerators is in the range of Watts for the warmer stages and in the micro-Watt range for colder stages. Based on our measured data, from a thermal point of view, thousands of DWG lines could be easily added to the setup without influencing the individual minimal stage temperature significantly. It is interesting to note, however, that the heat conductance of HDPE is comparable to stainless steel above the 45 K stage. At lower temperatures, its contribution to the overall heat load of a DWG with shielding is negligible, allowing for very efficient thermal isolation. In comparison to a coaxial solution, there is no inner wire, which is advantageous as well. The metallic body of the transition part can be bolted directly to the low temperature stage, which is a significant simplification especially at mK temperatures.

F. Signal conditioning

To thermalize the input signal we used the strategy known from the microwave experiments with superconducting qubits. Using dissipative elements, like the black DWG, the signal as well as the noise is attenuated at cold stages. Thus, the signal to noise ratio remains constant, but the (thermal) Nyquist contribution to the noise drops to the level of the individual temperature stages. Additional attenuation can be obtained by commercial WR10

attenuators, resistive WR10 tubes [14] or, as in our case, by adding a dissipative copper powder coating to the surface of the DWG, as shown in Fig.5. To character-

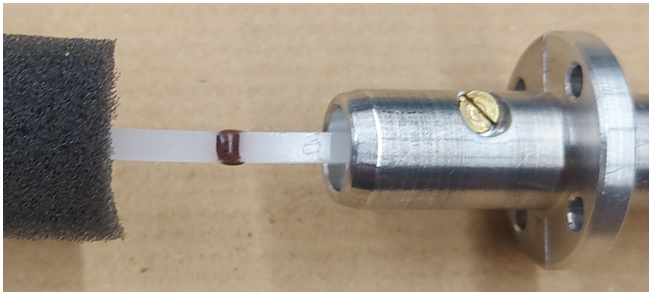


FIG. 5. Disassembled DWG with $\simeq 1$ mm copper coating for additional attenuation. The transparent DWG connects to a aluminum stage transition, shown on the right side.

ize the attenuation, we have measured the transmission (S21) of a transparent DWG with copper coating applied over a length of up to 65 mm in several steps. These measurements were conducted at room temperature. We observed that the attenuation is frequency independent and yields the loss of about 1 dB/mm in the range 85 - 110 GHz. The reflected signal S11 remained below -20 dB over the whole frequency range. From the low level of reflection, we conclude that the signal is mostly dissipated by the coupling of the evanescent wave to the copper powder coating. The copper coating could also be beneficial in other applications, e.g. to suppress standing waves in the cable caused, e.g., by imperfect impedance matching at the ends.

Similar to Refs. [14, 15], we amplify the signal transmitted through the lowest temperature stage by a factor of about 200 using a commercial wide-band cryogenic high electron mobility (HEMT) amplifier (LNF LNC_65_110WB) located at the 2.7 K temperature stage. To suppress parasitic resonances as well as back-action from the amplifier on the sample, a WR10 Faraday-type circulator (QuinStar QIF-W) is added at the input of the HEMT. On the room temperature side, we add two amplifiers (LNF-LNR65_115WD_SV, +29 dB each), leading to an overall signal boost of approximately +80 dB. In total, the attenuation from room temperature to the sample on the input line is in the order of 70 dB, which is sufficient for low photon number operation.

III. FABRY-PÉROT CAVITY

A. Design

We follow the general design of Ref. [16] to construct a Fabry-Pérot cavity (FPC) adapted to the frequency range of the setup (W-band), with some important differences discussed below. The FPC consists of two mirrors facing each other with vacuum space in between. We study two configurations, one with two spherical mirrors

and another one with a planar and a spherical mirror, see Fig. 6. The design considerations of a FPC are well known, so we will only briefly review some important points for the two configurations, see e.g. [17] for details. The condition for a cavity consisting of two (spherical) mirrors

$$0 < \left(1 - \frac{d}{R_1}\right) \cdot \left(1 - \frac{d}{R_2}\right) < 1 \quad (2)$$

determines the stability of a standing wave between the mirrors. Here, the distance between the mirrors is given by d and the radii of curvatures are R_1 and R_2 . Following this, one expects resonance frequencies for two curved mirrors with the same curvature when

$$f_{p,l,q} = \frac{c}{2d} \left(q + 1 + \frac{2p+l+1}{\pi} \arccos \left(1 - \frac{d}{R} \right) \right) \quad (3)$$

and for one planar and one curved mirror [18] under condition

$$f_{p,l,q} = \frac{c}{2d} \left(q + 1 + \frac{2p+l+1}{\pi} \arctan \left(\sqrt{\frac{d}{R-d}} \right) \right) \quad (4)$$

where c is the speed of light and p , l and q are the mode indices. The terms with the arccos and arctan functions are corrections due to the specific geometry of the cavity. The formulas above are related to the unperturbed cavity resonances, that is with no external signal coupling or mirror support structures. The coupling scheme, however, can have a strong influence on the individual modes and causes shifts of the observed resonance frequencies. One scheme often employed in the strong coupling regime $Q_c \sim 1000$ makes use of a small hole drilled through one of the mirrors and to measure the reflected signal. Since we are interested in coupling quality factors above $Q_c > 100\,000$, we decided for a different approach, as depicted in Fig. 6. Here, a WR10 waveguide is passing the cavity body next to the mirrors, with a hole connecting to the cavity. The diameter of the hole is smaller than the corresponding mode wavelength in the cavity. Assuming the hole to be a circular waveguide with a cutoff frequency $f_k \approx 146 - 160$ GHz [19], an evanescent wave can enter and leave the cavity with the signal fraction $A/A_0 = e^{\alpha l}$ and the attenuation

$$\alpha = \frac{2\pi f_k}{c} \sqrt{1 - \left(\frac{f}{f_k}\right)^2}. \quad (5)$$

With a hole diameter of 1.1-1.2 mm and a length l of 0.9 mm this leads to an in-out coupling of about -20 dB at 100 GHz.

Figure 8 shows a schematic of the FPC. All outer parts as well as the mirror bodies are made in-house from oxygen-free copper. The spherical mirrors have a radius of 25 mm and a center-to-center distance of 5.7 mm.

For the fabrication process of the niobium coated mirrors, we have taken the work [16] as a reference. First, the

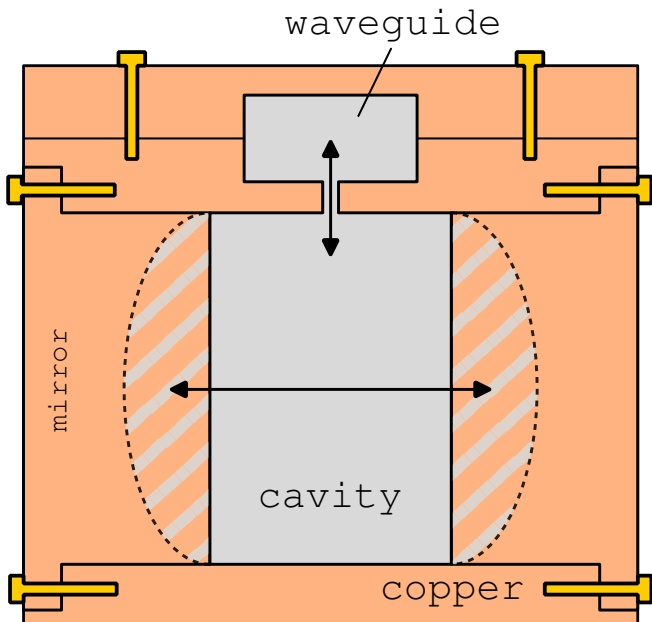


FIG. 6. Schematic of the Fabry-Pérot cavity (not to scale). Two mirrors (spherical or planar, see text) held in position by a copper support structure. The mm-wave signal of a hollow rectangular waveguide is coupled into the cavity by a hole smaller than the wavelength. Areas in grey depict the hollow volumes while copper parts are colored orange.

mirrors are machined from an oxygen-free copper block. After careful cleaning, they are annealed at 600 °C for 30 min in vacuum. Then, the mirrors are polished in several iterations using several diamond based polishing pastes and stainless steel matrix/pad with the inverse shape. We expect a residual surface roughness in the low μm range. Residuals of the polishing paste are removed with acetone and isopropanol. Finally, a 1 μm thick coating of niobium is deposited in an argon atmosphere by DC-magnetron sputtering under rotation. Without breaking the vacuum, we add a 5 nm capping of aluminum on top of the niobium coating to prevent oxidation of the niobium.

B. Characterization of the Fabry-Pérot cavity

One difference of a FPC in comparison to, e.g., a superconducting thin film resonator, is its broad and rich spectrum of modes described by Eqs. (3) and (4). Our coupling scheme leads to different coupling strengths of individual cavity modes to the waveguide, since it depends on the specific electromagnetic field amplitude in the vicinity of the hole.

Some modes with stronger coupling are already visible at room temperature and can be monitored during cool down and warm up. The frequency dependence of such a mode at around 112 GHz is shown in Fig. 7. We understand this behavior as an isometric thermal expansion of

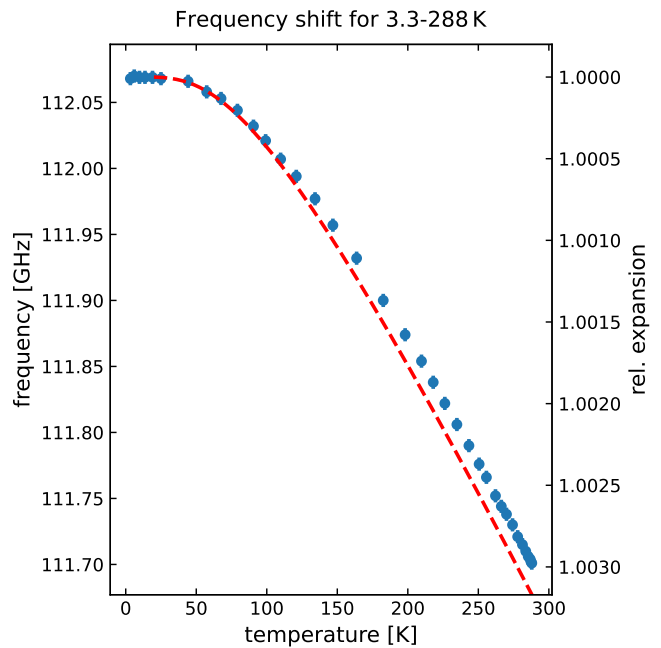


FIG. 7. Frequency shift of a FPC mode at 112 GHz between room temperature and 3.3 K. The red overlay (no fit) shows the relative expansion of copper based on tabulated values [20].

the mirror bodies and the support structure, and therefore a changing distance between the mirror surfaces. This leads to a strong temperature dependence with a shift of 370 MHz between 40 K and room temperature. Figure 7 also shows a comparison with tabulated values for the expansion coefficient of copper. At lower temperatures, the frequency dependence flattens out (~ 2 MHz shift), as expected.

At temperatures below 8 K, the superconducting state of the niobium coating ($T_c = 9.2$ K) becomes visible. A multitude of new modes appears with coupling quality factors ranging between 10^5 and 10^7 . A typical resonance curve in the weak coupling regime, measured at 2.5 K, is shown in Fig. 8. The mm-wave response of resonances are analyzed using a circle fit algorithm [21] which is implemented in the software package QKIT [22].

Figure 9 shows the temperature dependence of a resonance curve in the range from 2.5 K to 6.6 K, above this temperature the resonance becomes indistinguishable from noise. With decreasing temperature the resonance frequency shifts to higher values, which we attribute to the appearance of the superconducting energy gap. We observe a shift of the resonance dip of about 500 kHz at 6.6 K, which allows us to estimate a combined superconducting kinetic inductance fraction and residual thermal expansion of the cavity to be in the order of 10^{-5} . The amount of thermally activated quasi-particles is reduced with temperature decreasing, as indicated by the steep increase in the internal quality factor, shown in the inset.

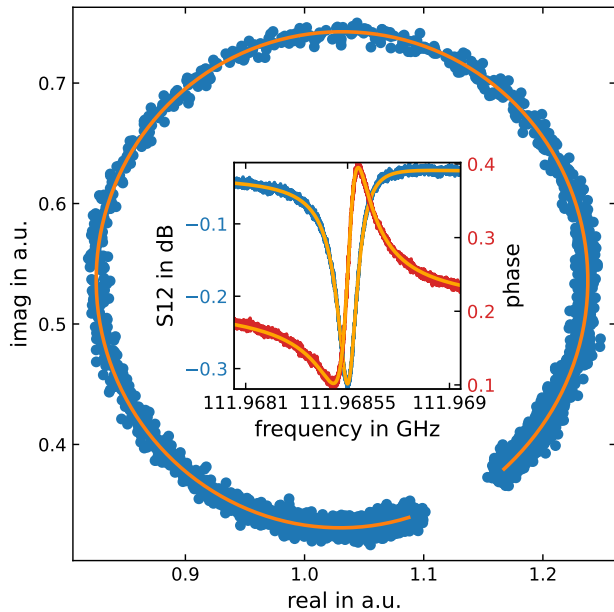


FIG. 8. The IQ-plane of a resonance measured at 2.4K for the FPC is shown, as well as amplitude and phase data in the inset. The internal and coupling quality factor for this particular resonance are $Q_i = 1.2 \cdot 10^6$ and $Q_c = 3.7 \cdot 10^6$.

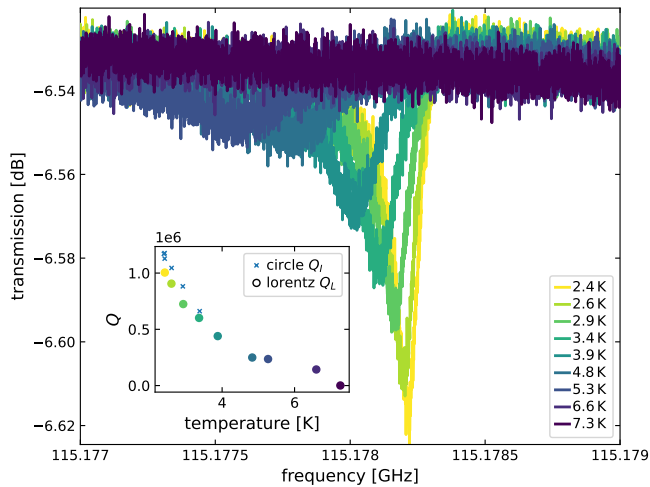


FIG. 9. Transmission measurement of a resonance at different temperatures. The insert shows the quality factors.

At temperatures of 10 mK, we observe several FPC modes in the few photon power limit with internal quality factors of about $2 - 3 \times 10^6$. The coupling quality factors vary between individual modes between 10^5 and 10^7 .

IV. CONCLUSION

We have demonstrated the feasibility of employing dielectric waveguides for measurements at milli-Kelvin temperatures and low photon numbers. The DWGs are simple to manufacture, they are flexible and have low losses as well as a low heat conductance. We have verified options to attenuate applied signals at the cryogenic stages with the use of black DWGs or added copper powder coating. The black DWG also efficiently attenuates infrared radiation. With the presented implementation, thousands of DWGs could be inserted to off-the-shelf dilution refrigerators without exceeding the thermal budget. Additional metallic shields can be used to suppresses the electromagnetic cross-talk between signal lines, which is mandatory at measurements at low photon numbers. We verify the performance of the system by measuring a transmission through a superconducting Fabry-Pérot cavity at around 100 GHz, which shows internal quality factors greater than 10^6 .

V. ACKNOWLEDGMENTS

We thank T. Zwick for fruitful discussions. This work was supported by funding from the European Research Council (ERC) under the European Union's Horizon 2020 research and innovation programme (project *Milli-Q*, grant agreement number 101054327).

Appendix A

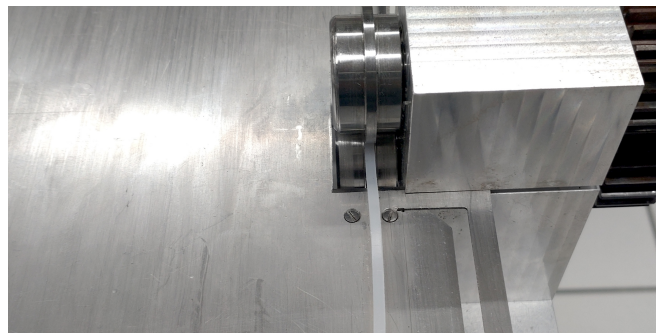


FIG. A.1. Image of the DWG cutting tool. The tool employs two sets of matrices. With the first, we cut the DWG from a 1.5 mm thick and 2 m long sheet of HDPE to a width of 2.5 mm. With the second set of matrices we roll it to a thickness of 1.3 mm while maintaining its width. We found that the transmission quality of the signal depends sensitively on the DWG homogeneity as well as the smoothness of the edge, i.e. a sharp cut.

-
- [1] D. Hondros and P. Debye, *Annalen der Physik* **337**, 465 (1910).
- [2] S. Fukuda, Y. Hino, S. Ohashi, T. Takeda, H. Yamagishi, S. Shinke, K. Komori, M. Uno, Y. Akiyama, K. Kawasaki, and A. Hajimiri, *IEEE Journal of Solid-State Circuits* **46**, 3113 (2011).
- [3] C. D’heer and P. Reynaert, *IEEE Journal of Solid-State Circuits* **59**, 889 (2024).
- [4] H.-T. Zhu, D. Liu, J. Hu, S. Li, S.-C. Shi, Q. Xue, and W. Che, *IEEE Transactions on Terahertz Science and Technology* **10**, 190 (2020).
- [5] C. Koenen, G. F. Hamberger, U. Siart, T. F. Eibert, H.-U. Nickel, G. D. Conway, and U. Stroth, *IEEE Transactions on Microwave Theory and Techniques* **66**, 128 (2018).
- [6] C. Macculi, M. Zannoni, O. A. Peverini, E. Carretti, R. Tascone, and S. Cortiglioni, *Appl. Opt.* **45**, 5168 (2006).
- [7] J. Weinzierl, Ch. Fluhrer, and H. Brand, in *1998 IEEE Sixth International Conference on Terahertz Electronics Proceedings. THZ 98. (Cat. No.98EX171)* (IEEE, Leeds, UK, 1998) pp. 166–169.
- [8] A. Hofmann, E. Horster, J. Weinzierl, L.-P. Schmidt, and H. Brand, in *33rd European Microwave Conference Proceedings (IEEE Cat. No.03EX723C)* (IEEE, Munich, Germany, 2003) pp. 955–958 Vol.3.
- [9] F. Pobell, *Matter and Methods at Low Temperatures* (Springer Berlin Heidelberg, 1996).
- [10] E. D. Marquardt, J. P. Le, and R. Radebaugh, “Cryogenic material properties database,” in *Cryocoolers 11*, edited by R. G. Ross (Springer US, Boston, MA, 2002) pp. 681–687.
- [11] A. G. Gibson, D. Greig, M. Sahota, I. M. Ward, and C. L. Choy, *Journal of Polymer Science: Polymer Letters Edition* **15**, 183 (1977).
- [12] M. Giles and C. Terry, *Physical Review Letters* **22**, 882 (1969).
- [13] D. Greig, *Cryogenics* **28**, 243 (1988).
- [14] A. Anferov, A. Suleymanzade, A. Oriani, J. Simon, and D. I. Schuster, *Phys. Rev. Appl.* **13**, 024056 (2020).
- [15] A. Suleymanzade, A. Anferov, M. Stone, R. K. Naik, A. Oriani, J. Simon, and D. Schuster, *Applied Physics Letters* **116**, 104001 (2020).
- [16] S. Kuhr, S. Gleyzes, C. Guerlin, J. Bernu, U. B. Hoff, S. Deléglise, S. Osnaghi, M. Brune, J.-M. Raimond, S. Haroche, E. Jacques, P. Bosland, and B. Visentin, *Applied Physics Letters* **90**, 164101 (2007).
- [17] H. Kogelnik and T. Li, *Proceedings of the IEEE* **54**, 1312 (1966).
- [18] J. Krupka, A. Cwikla, M. Mrozowski, R. N. Clarke, and M. E. Tobar, *IEEE Transactions on Ultrasonics, Ferroelectrics and Frequency Control* **52**, 1443 (2005).
- [19] H. Meinke, F. Gundlach, K. Lange, and K. Löcherer, *Taschenbuch der Hochfrequenztechnik* (Springer Berlin Heidelberg, 1986).
- [20] *NIST/SEMATECH e-Handbook of Statistical Methods*, accessed on November 08, 2024.
- [21] S. Probst, F. B. Song, P. A. Bushev, A. V. Ustinov, and M. Weides, *Review of Scientific Instruments* **86**, 024706 (2015).
- [22] “<https://github.com/qkitgroup/qkit>,” .